JOURNAL OF GEOPHYSICAL RESEARCH, VOL. 102, NO. B7, PAGES 15,403–15,417, JULY 10, 1997

Interaction of mantle plumes and migrating mid-ocean ridges: Implications for the Galápagos plume-ridge system

Garrett Ito

Department of Geology and Geophysics, School of Ocean and Earth Science and Technology
University of Hawaii, Honolulu

Jian Lin

Department of Geology and Geophysics, Woods Hole Oceanographic Institution, Woods Hole, Massachusetts

Carl W. Gable

Earth and Environmental Sciences, Los Alamos National Laboratories, Los Alamos, New Mexico

Abstract. We investigate the three-dimensional interaction of mantle plumes and migrating mid-ocean ridges with variable viscosity numerical models. Numerical models predict that along-axis plume width W and maximum distance of plume-ridge interaction x_{max} scale with $(Q/U)^{1/2}$, where Q is plume source volume flux and U is ridge full spreading rate. Both W and x_{max} increase with buoyancy number Π_b which reflects the strength of gravitational- versus plate-driven spreading. Scaling laws derived for stationary ridges in steady-state with near-ridge plumes are consistent with those obtained from independent studies of *Ribe* [1996]. In the case of a migrating ridge, the distance of plume-ridge interaction is reduced when a ridge migrates toward the plume because of the excess drag of the faster moving leading plate and enhanced when a ridge migrates away from the plume because of the reduced drag of the slower moving trailing plate. Given the mildly buoyant and relatively viscous plumes investigated here, the slope of the lithospheric boundary and thermal erosion of the lithosphere have little effect on plume flow. From observed plume widths of the Galápagos plume-migrating ridge system, our scaling laws yield estimates of Galápagos plume volume flux of 5-16 x 10^6 km^3 $m.y.^{-1}$ and a buoyancy flux of ~2 x 10^3 kg s^{-1}. Model results suggest that the observed increase in bathymetric and mantle-Bouguer gravity anomalies along Cocos Plate isochrons with increasing isochron age is due to higher crustal production when the Galápagos ridge axis was closer to the plume several million years ago. The anomaly amplitudes can be explained by a plume source with a relatively mild temperature anomaly (50°-100°C) and moderate radius (100-200 km). Predictions of the along-axis geochemical signature of the plume suggest that mixing between the plume and ambient mantle sources may not occur in the asthenosphere but, instead, may occur deeper in the mantle possibly by entrainment of depleted mantle as the plume ascends from its source.

Introduction

A wide range of geologic and geochemical observations provide strong evidence that mantle plumes feed material to nearby mid-ocean ridges [e.g., *Vogt*, 1971; *Schilling*, 1973; *Schilling et al.*, 1976; *Morgan*, 1978]. Near-ridge plumes are documented to generate along-axis geophysical anomalies of widths exceeding 2000 km [*Ito and Lin*, 1995b] and can induce geochemical signatures at plume-ridge separation distances approaching 1400 km [*Schilling*, 1991]. The "mantle-plume source/migrating ridge sink" model of *Schilling* [1985; 1991] and *Schilling et al.* [1985] suggests that migrating ridges are "fed and dynamically affected by a preferential plume flow along a thermally induced channel at the base of the lithosphere" [*Schilling*, 1991]. As consistent with *Morgan's* [1978] hypothesis, *Schilling* [1985; 1991] and *Schilling et al.* [1985] suggest that a thermal channel is progressively carved into the lithosphere as a ridge migrates over and away from an impinging hot plume. In support of this model, all of the 13 plume ridge systems considered by *Schilling* [1991] have ridges migrating away from their nearby plumes.

Recent numerical modeling and laboratory experimental studies have begun to characterize the kinematic and dynamic aspects of interaction between mantle plumes and stationary mid-ocean ridges. For ridge-centered plumes, scaling laws for the dependence of along-axis plume width W on plume volume flux Q and ridge full spreading rate U were first explored in tank experiments [*Feighner and Richards*, 1995] and further developed in numerical studies [*Feighner et al.*, 1995; *Ribe et al.*, 1995; *Ito et al.*, 1996]. The dynamics of off-axis plumes were first investigated in the laboratory by *Kincaid et al.* [1995a] and in two-dimensional (2-D) numerical experiments by *Kincaid et al.* [1995b]. Finally, *Ribe's* [1996] study of off-ridge plumes and stationary ridges established scaling laws for the dependence of W on a range of variables including Q, U, plume-ridge distance x_p, and lithospheric thickening with age.

Paper number 97JB01049.
0148-0227/97/97JB-01049$09.00

While the above studies established scaling laws for plumes and stationary ridges, they did not investigate the effects of ridge migration. In the more realistic case of a migrating ridge, not only may thermal thinning of the lithosphere be important as envisioned by *Schilling* [1985; 1991] and *Schilling et al.* [1985], but also the plate trailing the migrating ridge typically moves slower relative to the plume than the plate leading the ridge axis thereby inducing less drag on the plume away from the ridge [*Ribe*, 1996; *Ribe and Delattre*, 1996].

We explore here the dynamics of plumes and migrating ridges with three-dimensional (3-D) numerical models that include thermal diffusion and fully pressure- and temperature-dependent mantle rheology. We will first establish scaling laws for along-axis plume width W and maximum plume-ridge interaction distance x_{max} for steady state systems of stationary ridges. These results will be compared with those of the constant viscosity plume models of *Ribe* [1996] to quantify the importance of thermal diffusion and variable plume viscosity on the scaling laws. We will then quantify the effects of ridge migration on W and x_{max}. Finally, we will compare model predictions with geophysical observations of the Galápagos plume-migrating ridge system and discuss the implications for the dimensions, temperature anomaly, fluxes, and geochemical signature of the Galápagos plume.

Governing Equations and Numerical Method

The mantle is modeled as a viscous Boussinesq fluid of zero Reynolds number and infinite Prandtl number. The equilibrium equations include conservation of mass

$$\nabla \bullet \boldsymbol{u} = 0, \tag{1}$$

momentum

$$\nabla \bullet \tau = \Delta \rho \mathbf{g}, \tag{2}$$

and energy

$$\frac{\partial T}{\partial t} = \kappa \nabla^2 T - \boldsymbol{u} \bullet \nabla T \tag{3}$$

(see *Ito et al.* [1996] for further details and Table 1 for definition of variables). Mantle density ρ is reduced by thermal expansion such that $\Delta\rho = \rho_0 \alpha \Delta T$, and the 3-D stress tensor τ depends on the strain rate tensor $\dot{\varepsilon}$ according to $\tau = 2\eta\,\dot{\varepsilon} - p\boldsymbol{I}$, where $\boldsymbol{I}$ is the identity matrix. Viscosity η depends on pressure p and real temperature T_R according to

$$\eta = \eta_0 \exp\left\{\frac{E+pV}{RT_R} - \frac{E+\rho_0 g(0.5D)V}{RT_{R0}}\right\} \tag{4}$$

[e.g., *Christensen*, 1984] in which T_{R0} is the real temperature

Table 1. Notation

Variable	Meaning	Value	Units
B	buoyancy flux		kg s^{-1}
c_p	specific heat	10^3	J kg^{-1} °C^{-1}
D	fluid depth	400	km
E	activation energy	1.9×10^5	J
g	acceleration of gravity	9.8	m s^{-2}
M	melt fraction		wt %
p	pressure		Pa
P	plume tracer concentration		
Q	volumetric plume flux		km^3 m.y.$^{-1}$
Q_r	fraction of plume flux crossing the ridge		
R	gas constant	8.314	J K^{-1} mol^{-1}
S_0	characteristic plume thickness	$(48Q\eta_p/g\Delta\rho)^{1/4}$	km
ΔS	entropy change on melting	400	J kg^{-1} °C
T	mantle potential temperature		°C
T_R	mantle real temperature		K
ΔT_p	plume temperature anomaly		°C
$\boldsymbol{u}$ (u,v,w)	mantle flow rate vector		km m.y.$^{-1}$
U	ridge full spreading rate		km m.y.$^{-1}$
V	activation volume	4×10^{-6}	m^3
W	along-axis plume width		km
W_0	plume width scale	$(Q/U)^{1/2}$	km
x_p	plume-ridge distance		km
x_{max}	maximum distance of plume-ridge interaction		km
X	melt depletion		wt %
α	coefficient of thermal expansion	3.4×10^{-5}	K^{-1}
β	coefficient of depletion density reduction	0.024	
γ	η_0/η_p		
κ	thermal diffusivity	31	km^2 m.y.$^{-1}$
η	viscosity		Pa s
η_0	reference viscosity		Pa s
η_p	plume viscosity at $0.5D$		Pa s
Π_b	buoyancy number	$Q\sigma/U^2$	
Π_u	upslope number	$Q^{1/8}\sigma^{3/8}\kappa^{1/2}/0.5U$	
ρ	mantle density		kg m^{-3}
ρ_0	mantle reference density	3300	kg m^{-3}
σ	buoyancy scaling parameter	$g\Delta\rho/48\eta_p$	m^{-1} s^{-1}
τ	stress tensor		Pa

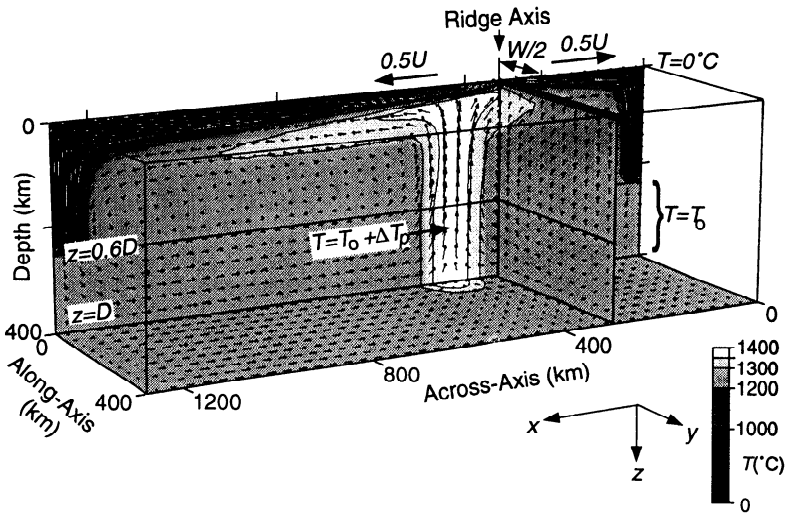

Figure 1. Perspective diagram showing mantle flow (small arrows of lengths proportional to velocity) and temperature (contoured and shaded) of an example model calculation with ΔT_p = 100°C and U = 60 km m.y.$^{-1}$ (experiment 8, Table 2). The ridge axis is located at x = 320 km and the plume source is centered at x = 450 km. The maximum vertical velocity is 115 km m.y.$^{-1}$ Both top (z = 0) and bottom ($z = D$) boundaries are isothermal planes except at the bottom of the plume source. The bottom boundary is shear stress free, and the top is fixed at horizontal velocities of +0.5U at x > 320 km and -0.5U at x < 320 km. The vertical sides of the box are reflecting, having zero horizontal temperature gradient and shear stress; therefore, by symmetry, this half plume-ridge system in numerical models simulates a full plume-ridge system. All boundaries are closed to flow both in and out of the numerical box, thus material flows downward at the ends of the box and recirculates toward the ridge axis along the base of the box. The effect of this recirculation on plume-ridge interaction is insignificant. The purpose of the lower volume of the box is to simulate an open boundary at the base of the upper volume where plume-ridge interaction occurs.

of the mantle at z = 0.5D. To simulate numerically the behavior of a non-Newtonian rheology (i.e., $\dot{\varepsilon} \propto \tau^3$), we used values of R and V that are reduced relative to experimentally derived values [*Christensen*, 1984]. To ensure numerical accuracy of the flow solutions, we set a maximum lithospheric viscosity such that the horizontal viscosity variation was $\leq 10^3$. The ratio of ambient/plume viscosity γ is defined as η_0/η_p, where η_p is the viscosity of the plume at z = 0.5D.

Calculations were done using the Cartesian numerical code first written by *Gable* [1989] and *Gable et al.* [1991] and later modified by *Ito et al.* [1996] to incorporate variable viscosity. The numerical setup is illustrated in Figure 1. Two spreading plates were simulated by imposing surface horizontal velocities of u_x = +0.5U and u_x = -0.5U on both sides of a model ridge axis. Temperature at the surface was maintained at 0°C causing a high-viscosity lithosphere to thicken approximately with the square root of distance from the ridge axis. Temperatures in the lower portion of the box (z > 0.6D) were maintained at the reference mantle potential temperature T_0 everywhere except inside the plume source. We thus solved the energy equation in only the upper portion of the box (0.6D ≥ z ≥ 0) where plume-ridge interaction occurs.

To generate a plume, we imposed a columnar-shaped temperature anomaly in the lower portion of the box (i.e., 0.6D < z ≤ D) at a distance x_p from the ridge axis. The plume source was defined to be hottest ($T = T_0 + \Delta T_p$) at its center and to cool as a Gaussian function of radial distance to T_0 at its full radius. Temperature anomaly ΔT_p and plume radius were input source properties, while plume volume flux Q was a model output, resulting naturally from the governing equations and experimental boundary conditions. We measured Q by integrating vertical velocities at the top of the imposed source column (z = 0.6D) over its cross-sectional area.

To track the flow of the mantle plume, we introduced a passive tracer P in the plume source with the value of 1.0 to represent 100% plume material. A finite difference, tensor diffusion method [*Gable*, 1989; *Travis et al.*, 1990] was used to solve for advection of P from the source and throughout the upper volume of the box (z < 0.6D). While this method has the advantage of being computationally efficient, its primary disadvantage is that it requires some diffusion of P. Thus, constrained by numerical limitations, we were able to reduce the rate of diffusion of P by a factor of 3 relative to that of thermal diffusion. We used P to determine the along-axis width of the plume by measuring the along-axis distance over which the mean value of P beneath the ridge,

$$1/0.6D \int_0^{0.6D} P(x,y,z)\mathrm{d}z,$$

was greater than 0.1. P was also used in steady state stationary ridge cases to measure the volume flux of plume material crossing the ridge axis Q_r by integrating horizontal velocities on the side of the ridge opposite the plume where P > 0.4. By using P > 0.4 as our criterion for measuring Q_r, we obtained Q_r values in ridge-centered plume experiments with a standard deviation of 8% of the desired value of 0.5.

Scaling Laws

Stationary Ridges

Feighner and Richards [1995] and *Feighner et al.* [1995] demonstrated that $W_0 = (Q/U)^{1/2}$ is an effective length scale for

Table 2. Experimental Parameters and Scaling Quantities

Run	U'/U, km m.y.$^{-1}$	ΔT_p, °C	γ	Π_b	Q'/Q, 10^6 km^3 m.y.$^{-1}$	W_0'/W_0, km	$W'(x_p=0)$ / $W(x_p=0)$, km
1	516 / 40	100	1.00	0.61	55 / 0.68	0.33 / 130	0.63 / 250
2	774 / 60	100	1.00	0.29	58 / 0.72	0.27 / 110	0.56 / 225
3	1290 / 100	100	1.00	0.11	64 / 0.79	0.22 / 89	0.50 / 200
4	387 / 30	200	1.00	3.97	100 / 1.24	0.51 / 203	1.00 / 400
5	774 / 60	200	1.00	1.04	105 / 1.29	0.37 / 146	0.75 / 300
6	1290 / 100	200	1.00	0.39	112 / 1.36	0.29 / 117	0.63 / 250
7	516 / 40	100	2.35	1.42	54 / 0.67	0.32 / 130	0.69 / 275
8	774 / 60	100	2.35	0.67	57 / 0.71	0.27 / 109	0.63 / 250
9	1290 / 100	100	2.35	0.26	61 / 0.75	0.22 / 87	0.50 / 200
10	387 / 30	200	5.05	15.05	150 / 1.86	0.62 / 249	1.65 / 660
11	774 / 60	200	5.05	6.10	123 / 1.53	0.40 / 160	0.94 / 375
12	1290 / 100	200	5.05	2.30	127 / 1.58	0.31 / 126	0.75 / 300

Primes denote dimensionless quantities and are listed adjacent to their scaled quantities. Source radius is 50 km. Input parameters are U, ΔT_p, and rheology law. The remaining quantities are model output (see text). Runs 4 and 10 have numerical box dimensions 3.2D x 2.0D x 1.0D with 128 x 64 x 50 grids in x, y, and z, respectively. The other runs have box dimensions 3.2D x 1.0D x 1.0D with 128 x 32 x 50 grids in x, y, and z, respectively. Rayleigh number is 1.83 x 10^6 based on T_0= 1300°C and η_0 = 5 x 10^{19} Pa s.

characterizing the horizontal dimension of a ridge-centered, gravitational spreading plume. They also defined a plume buoyancy number $\Pi_b = Q\sigma/U^2$, where $\sigma = g\Delta\rho/48\eta_p$, which characterizes the relative strength of gravitational versus plate-driven spreading. *Ribe* [1996] and *Sleep* [1996] characterized the effect of the sloping lithosphere on the interaction of off-axis plumes by an "upslope number" $\Pi_u = Q^{1/8}\sigma^{3/8}\kappa^{1/2}/0.5U$, which is the ratio of lithospheric thickness (i.e., at a distance $L_0 = Q^{3/4}\sigma^{1/4}/0.5U$ from the ridge axis) to characteristic plume thickness $S_0 = (Q/\sigma)^{1/4}$.

The above scaling quantities were shown by lubrication theory models of *Ribe* [1996] to define a scaling law of W for steady-state stationary ridges,

$$W = W_0 F_1(\Pi_b) F_4(\Pi_b, \Pi_u) F_3\left(\frac{x_p}{W_0}, \Pi_b, \Pi_u\right). \quad (5)$$

This general form of the scaling law is composed of four functions which describe the dependence of W on the variables Π_b, Π_u, and plume-ridge separation distance x_p. Functions F_1, defined by $\log_{10}(F_1) = 0.368 + 0.0569[\log_{10}(4\Pi_b)] + 0.0176[\log_{10}(4\Pi_b)]^2 + 0.0275[\log_{10}(4\Pi_b)]^3$, and $F_4 = (1 + 1.77\ \Pi_u\ (4\Pi_b)^{-0.33})$ together describe the increase in W with increasing Π_b and Π_u for ridge-centered plumes ($x_p = 0$). Function

$$F_3 = \left[1.0 - 0.625\left(\frac{x_p}{W_0 F_2 (1 - 0.34\Pi_u^{0.30})}\right)^2\right]^{1/2}$$

describes the dependence of W on x_p for off-axis plumes ($x_p \neq 0$), where F_2 is defined by $\log_{10}(F_2)$=$0.043[\log_{10}(4\Pi_b)] + 0.060[\log_{10}(4\Pi_b)]^2 - 0.0062[\log_{10}(4\Pi_b)]^3$. We now further investigate this scaling law with numerical models that include both thermal diffusion and temperature-dependent plume viscosity.

In numerical experiments, we varied full spreading rate U between 20 and 120 km m.y.$^{-1}$ and changed plume flux Q by varying plume temperature anomaly ΔT_p between 100° and 200°C (see Table 2). Three models of plume viscosity structure were examined. The first was designed to simulate the constant plume-viscosity calculations of *Ribe* [1996]. This viscosity structure includes the temperature dependence of (4) for $T < T_0$ to allow for a thickening lithosphere but has $\eta = \eta_0$ for $T \geq T_0$ (i.e., γ= 1.0) and omits the pressure-dependence effect. The second and third viscosity models have the full pressure and temperature dependence as defined by (4); the second has γ = 2.352 for ΔT_p = 100°C, and the third has γ = 5.053 for ΔT_p = 200°C.

In the case of a ridge-centered plume, $x_p = 0$ and $F_3 = 1.0$, and thus W depends only on functions F_1 and F_4. A scaling law for normalized plume width W/W_0 was determined by fitting numerically determined values of W/W_0 to exponential functions of Π_b. $F_1F_4 = W/W_0$ can be described by the function

$$\log_{10}(F_1F_4) = \log_{10}(W/W_0) =$$
$$0.32 + 0.01[\log_{10}(\Pi_b)] + 0.05[\log_{10}(\Pi_b)]^2 \quad (6)$$

with a standard deviation misfit of 8% of the median value of 2.25 (Figure 2). Owing to numerical limitations, we investigated only small values of Π_u over a limited range of 0.04–0.4. Consequently, we did not detect any effects of lithospheric slope on our numerical results (*Ribe*'s [1996] function F_4 predicts only a ~12% variation in W over this range of Π_u). Equation (6) thus defines our function F_1, which is consistent in general form with *Ribe* 's [1996] function F_1 (Figure 2).

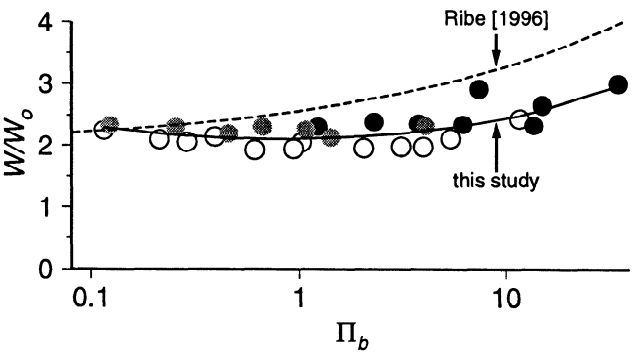

Figure 2. Numerical results of along-axis plume width W, scaled by $W_0 = (Q/U)^{1/2}$, versus buoyancy number Π_b. Experimental parameters are γ = 1.0 and ΔT_p = 100°C and 200°C (open circles), γ = 2.35 and ΔT_p = 100°C (shaded circles), and γ = 5.05 and ΔT_p = 200°C (solid circles). Solid curve shows the best fitting scaling law described by equation (6). Dashed curve is predicted by *Ribe* [1996].

Two inconsistencies, however, are evident between our results and those of *Ribe* [1996] (Fig 2): 1) our values for F_1 are on average ~25% less than those of *Ribe* [1996], and (2) at low values of Π_b, the slope of our function F_1 is slightly negative, while the slope of *Ribe*'s [1996] function remains positive. The difference in amplitudes of our functions and those of *Ribe* [1996] can be accounted for largely by the fact that because we define Π_b based on the maximum plume temperature anomaly ΔT_p, we may overestimate the effective Π_b by a factor of 2-4 since the average temperature of the plume is less than ΔT_p. This effect would shift our curve in Figure 2 to smaller values of Π_b thus bringing our function into better agreement with *Ribe's* [1996]. The negative slope in our function F_1 for Π_b <1 most likely reflects a second-order dependence on plume radius when radius exceeds ~20% of W. Additional numerical tests confirmed that W/W_0 tends to increase with plume radius for radii >17-20% of W. *Ribe's* [1996] study only considered cases in which the plume source radius <<W.

For off-axis plumes, $x_p \neq 0$, and thus W depends on an additional function $F_3(x_p)$. Figure 3 illustrates the shape of the plume at different distances from the ridge axis. When a plume is off axis, it spreads asymmetrically beneath the moving plate; as x_p increases, the ridge captures a narrower width of the plume. If x_p is large enough, the ridgeward flowing plume material stagnates against the migrating plate before it reaches the ridge axis. It is this stagnation distance that defines the maximum distance x_{max} to which plume material will contact the ridge axis.

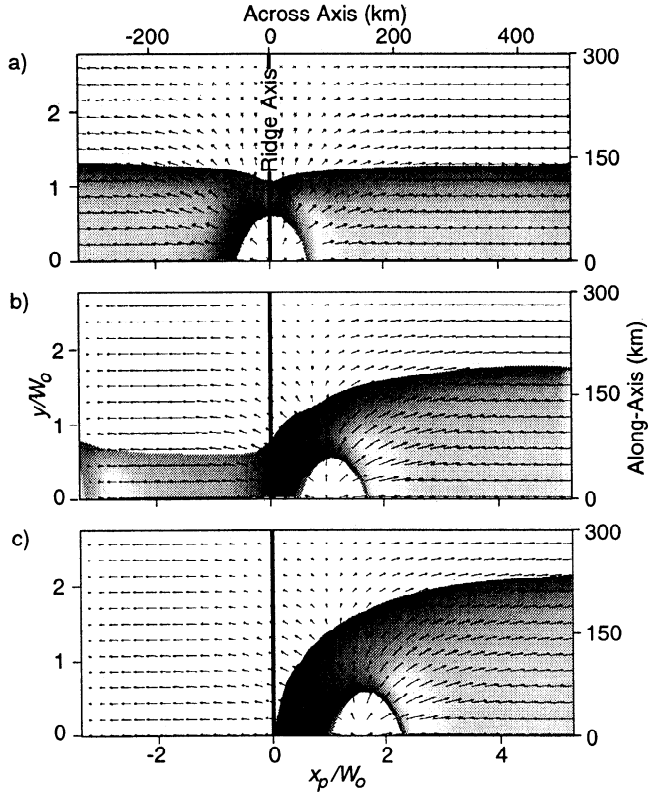

Figure 3. Steady state isosurface of plume tracer, $P = 0.4$, as viewed from the bottom of the numerical modeling box looking upward. Shading denotes illumination from the right of Figure 3. Small arrows illustrate horizontal velocities at z = 64 km. The ridge axis is marked by the bold line. Results are from experiment 8 (Table 2). (a) Plume-ridge distance $x_p = 0$ km or $x_p/W_0 = 0$, (b) x_p = 100 km or $x_p/W_0 = 0.93$, and (c) x_p = x_{max} = 150 km or $x_p/W_0 = 1.39$. Note that the plume width at the ridge axis decreases with increasing x_p.

The dependence of W on x_p is described by the best fitting function

$$F_3 = [1.0 - 0.68(x_p/W_0F_2)^2]^{1/2}, \quad (7)$$

which is very similar to results of Ribe [1996] (Figure 4b). As evident in Figure 4a, cases with $\gamma = 1.0$ yield the shortest distances of plume-ridge interaction, whereas increasing γ results in greater distances of plume-ridge interaction. This behavior reflects a stretching function F_2, which depends primarily on γ and secondarily on Π_b with a best fitting function

$$F_2 = \Pi_b^{0.01}\gamma^{0.14}. \quad (8)$$

As illustrated in Figure 4b, incorporating F_2 in (7) collapses values of $W/W(x_p = 0)$ onto a single curve. Our definition of F_2 captures the linear exponential term of *Ribe*'s [1996] function; however, our results show a weaker dependence on Π_b. We again do not observe a significant dependence on Π_u over the limited range of Π_u examined.

Similar to along-axis width W, the percentage of the plume flux that crosses the ridge axis Q_r also decreases with increasing x_p. With increasing values of x_p, Q_r decreases from 0.50 when $x_p = 0$ to zero when $x_p = x_{max}$, according to

$$Q_r = 0.50 - 0.41(x_p/W_0F_2) \quad (9)$$

(Figure 4c). Accordingly, the maximum distance of plume-ridge interaction x_{max} occurs when functions F_3 and Q_r are zero and therefore

$$x_{max} = 1.22W_0F_2. \quad (10)$$

Equation (9) is consistent with *Ribe's* [1996] results of Q_r = $0.50-0.56(x_p/W_0F_2) + 0.12(x_p/W_0F_2)^2$ (Figure 4b) and (10) is consistent with *Ribe's* [1996] function, $x_{max} = 1.26W_0F_2$ for $F_4 = 1$. The similarities between our scaling laws (equations (6)-(10)) for steady-state stationary ridges and those of *Ribe* [1996] indicate that the general form of these scaling laws are robust and insensitive to plume source radii for (radii <~20% of W) and differences in far-field boundary conditions. In addition, these similarities suggest that variable plume viscosity has only second-order effects on plume-ridge interaction.

Migrating Ridges

To derive scaling laws for systems in which the ridge migrates parallel to the direction of plate spreading, we simulated a ridge moving in the positive x direction at a velocity of V_r relative to the plume source. With respect to the ridge axis, both plates were assumed to spread symmetrically at a rate of $0.5U$. Therefore with respect to the plume, the leading plate, moving in the positive x-direction (plate 1), spreads with a velocity of $+0.5U + V_r$, and the trailing plate, moving in the negative x direction (plate 2), spreads with a velocity of $-0.5U + V_r$ (Figure 5).

Numerical experiments began with the steady state configuration of a stationary ridge and a plume beneath plate 1 at a plume-ridge distance $x_p > x_{max}$. We then allowed the ridge to migrate toward, over, and away from the plume such that the plume ended up beneath plate 2. We used the conventions, $x_p > 0$ when the plume is beneath plate 1 and $x_p < 0$ when the plume is beneath plate 2. Three ridge migration velocities were considered together with parameters of experiments 3, 5, 7, 8, and 12 (Table 2). In each case, the maximum V_r examined was equal to the half spreading rate.

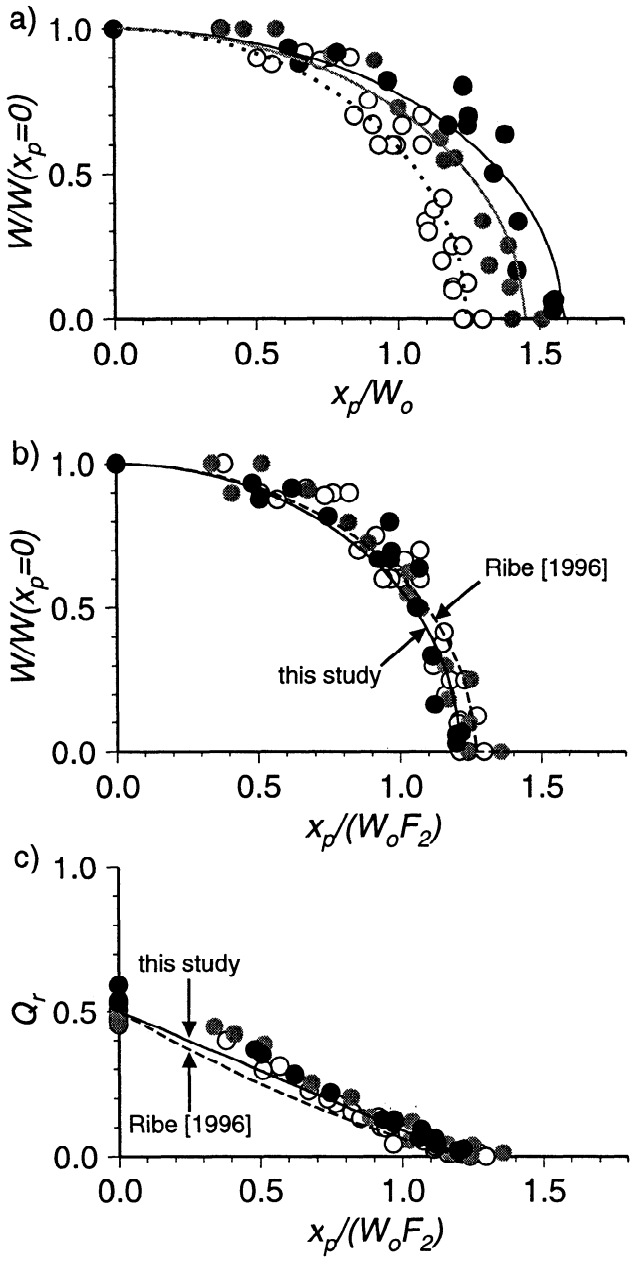

Figure 4. (a) Numerical results of along-axis plume width W, scaled by the width for $x_p = 0$, versus plume-ridge distance x_p, scaled by W_0. Experimental parameters are $\gamma = 1.0$ (open circles), $\gamma = 2.35$ (shaded circles), and $\gamma = 5.05$ (solid circles). The best fitting curves based on equation (7) are shown for $\gamma = 1.0$ (dotted), $\gamma = 2.35$ (shade), and $\gamma = 5.05$ (solid). (b) Similar to Figure 4a but the plume-ridge distance x_p is scaled by W_0F_2. Using this scaling law, all experimental results collapse onto a single curve. The standard deviation misfit between experimental results and best fitting solid curve equation (8) is 0.13. (c) Fraction of plume flux crossing the ridge axis Q_r versus $x_p/(W_0F_2)$. The standard deviation misfit of the best fitting curve (equation (9)) is 0.08. The mismatches to numerical results for $x_p/(W_0F_2) \leq \sim 1.0$ in both Figures 4b and 4c indicate possible dependence on higher-order terms of x_p that we did not attempt to resolve. At $x_p = 0$, the mean value is 99.2% of the correct value of 0.5; the standard deviation of ~8% reflects the inaccuracy in measuring Q_r caused by numerical diffusion of P. Dashed curves in (b) and (c) are functions obtained by *Ribe* [1996].

The dependence of W on x_p for migrating ridges is shown in Figure 6 for experiment 8, as described by

$$F_3 = W/W(x_p=0,\ V_r=0) = \left[1.0 - 0.68F_6(s,\Pi_b)\left(\frac{x_p / W_0 + F_5(s,\Pi_b)}{F_2(\Pi_b)}\right)^2\right]^{1/2}, \quad (11)$$

where $s = V_r/0.5U$. The first effect of V_r on W is to shift the curve of $W/W(x_p = 0, V_r = 0)$ in the negative x_p direction (Figure 6). This effect is best described by the function

$$F_5 = 0.38\Pi_b^{-0.12}(V_r/0.5U)^{1/2} \quad (12)$$

(Figure 7a). The second effect of V_r is to increase the total horizontal range over which the plume interacts with the ridge and is described by the function

$$F_6 = 1.0 - 0.16\Pi_b^{-0.12}(V_r/0.5U)^{1/2} \quad (13)$$

(Figure 7b).

Together, functions F_5 and F_6 reflect the kinematic and dynamic behavior of a gravitationally spreading plume subject to the differential shearing conditions of the two lithospheric plates. When $x_p > 0$, the faster moving plate 1 induces more drag on the plume away from the ridge (Figure 5a) therefore pushing the stagnation point closer to the plume source and reducing x_{max} relative to the case in which $V_r = 0$. When $x_p < 0$, the slower moving plate 2 induces less shear away from the ridge (Figure 5b); consequently, ridgeward spreading of the plume is able to keep pace with the migrating ridge over a greater distance. For ridges migrating toward a plume at $V_r \sim 0.5U$, our models predict plume-ridge interaction distance to decrease by ~25% relative to that of a stationary ridge. On the other hand, for ridges migrating away from plumes at $V_r \sim 0.5U$, we predict plume-ridge interaction distance to increase by ~35% relative to that of a stationary ridge and almost 100% of that for a ridge migrating toward a plume. Similar conclusions were obtained by *Ribe and Delattre* [1996], who investigated plume-migrating-ridge interaction using lubrication theory. Our function F_5 is analogous to function B of *Ribe and Delattre* [1996], which, like F_5, increases with increasing V_r. Likewise, F_6 is analogous to *Ribe and Delattre's* [1996] function $1/C$, which, like F_6, decreases with increasing V_r over the range of Π_b values that we have considered.

Thus our complete scaling law for along-axis plume width that includes the effects of ridge migration parallel to plate spreading is

$$W = W_0 F_1(\Pi_b)\left[1.0 - 0.68F_6(s,\Pi_b)\left(\frac{x_p / W_0 + F_5(s,\Pi_b)}{F_2(\Pi_b)}\right)^2\right]^{1/2}. \quad (14)$$

The corresponding scaling law for the maximum plume-ridge interaction distance is

$$x_{max} = (\pm 1.22F_2F_6^{-1/2} - F_5)W_0. \quad (15)$$

In the numerical models presented in this paper as well as in separate numerical tests, we were unable to detect any effects of lithospheric erosion on the flow of the plume. This is because the mild plume temperature anomalies we investigated generate plumes with characteristic thicknesses too great to be influenced by the shape of the overlying, relatively thin lithosphere. As shown in Figure 8, the amount of thermal cro-

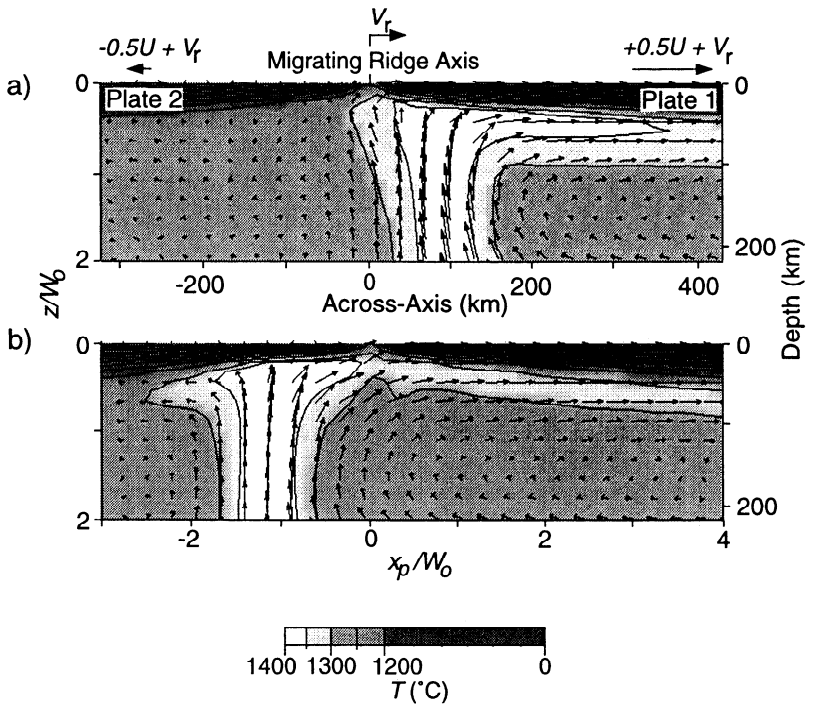

Figure 5. Mantle flow (arrows of lengths proportional to velocity) and temperature (contoured and shaded) in across-axis vertical sections through the center of the plume source ($y = 0$) for experiment 8 (Table 2). (a) Ridge axis is migrating toward the plume which is beneath the faster moving plate 1. (b) Ridge axis is migrating away from the plume which is beneath the stationary plate 2.

sion between the plume and ridge is less than ~6% of the characteristic plume thickness $S_0 = (48Q\eta_p/g\Delta\rho)^{1/4}$, regardless of how fast the ridge migrates. We find that thermal erosion occurs primarily by differential conductive cooling rates between plume-affected and normal lithosphere and that mechanical erosion by the plume is small. Consistent with arguments of *Sleep* [1996], we thus find that the amount of thermal erosion increases with duration that the lithosphere is in contact with the plume (Figure 8). In the portion of the plate between the plume and ridge, this contact duration is lithospheric age which is independent of ridge migration rate. Downwind of the plume, the area of erosion reflects the time since plume material crossed the ridge from plate 1 to plate 2. In the case in which $V_r = 0$ (Figure 8a), the whole downwind region of the plate has been heated by the plume and thus the area of erosion is large. In the case in which $V_r = 0.5U$ (Figure 8d), however, erosion is more confined to the plume because the plume only recently crossed the ridge. Our results are consistent with the study of *Ribe and Delattre*'s [1996], who find that lithospheric erosion contributes only second-order effects on plume flow.

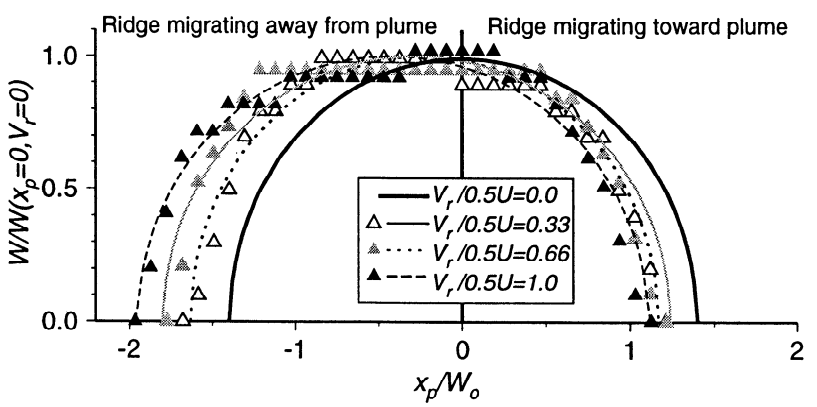

Figure 6. Numerical results of along-axis plume width W, scaled by $W(x_p = 0, V_r = 0)$ versus plume-ridge distance x_p, scaled by W_0. Plate half spreading rate is $0.5U$ = 30 km m.y.$^{-1}$. Bold curve shows the prediction for stationary ridges ($V_r = 0$) based on equation (7). Experimental results (triangles) are shown with best fitting functions from equation (11) (curves): $V_r/0.5U = 0.33$ (open triangles and dotted line); $V_r/0.5U = 0.66$ (shaded triangles and shaded line); $V_r/0.5U = 1.0$ (solid triangles and dashed line). Mismatches are largest near the apexes of each curve, which may be partially due to difficulty in resolving small changes in W and partially due to possible dependence of W on higher-order terms of x_p that we did not attempt to resolve.

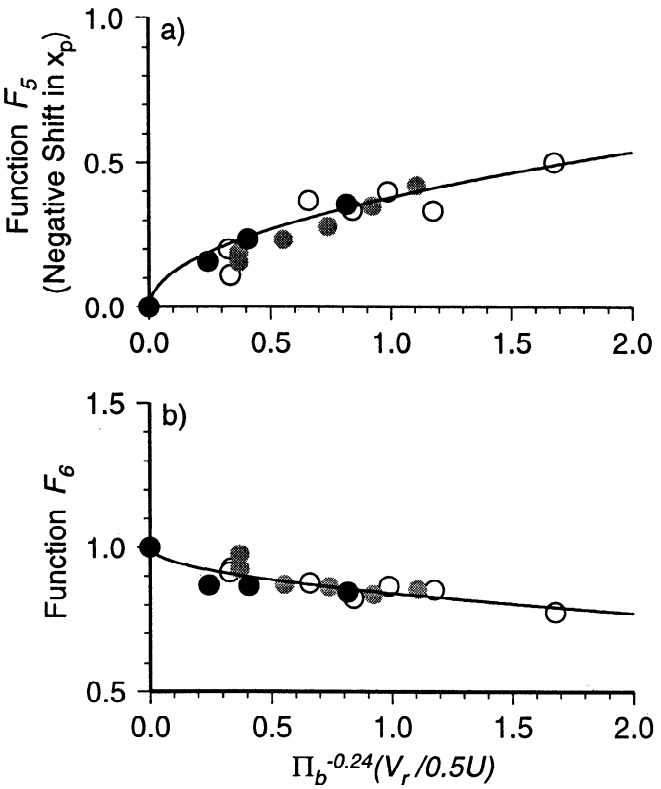

Figure 7. (a) Numerical results showing dependence of function F_5 on Π_b and $V_r/0.5U$. Experimental parameters are: γ= 1.0 (open circles), γ = 2.35 (shaded circles), and γ = 5.05 (solid circles). Solid line shows best fitting function based on equation (12). (b) Numerical results showing dependence of function F_6 on Π_b and $V_r/0.5U$. Symbols are the same as in Figure 7a. Solid line shows best fitting function based on equation (13).

Galápagos Plume-Migrating Ridge System

The Galápagos is a relatively well-studied example of a plume-migrating ridge system (Figure 9). The Galápagos Spreading Center lies ~200 km north of the Galápagos Archipelago, the western end of which marks the current location the Galápagos plume [e.g., *Hey*, 1977; *Morgan*, 1978]. At present day, the ridge axis is migrating northward with respect to the hotspot at a rate of ~27 km m.y.$^{-1}$ [*Gripp and Gordon*, 1990], which is ~1 km m.y.$^{-1}$ less than the half spreading rate at 91°W [*DeMets et al.*, 1994]. Analyses by *Ito and Lin* [1995a] demonstrated that the along-axis shallowing of the Galápagos ridge axis coincides with a mantle-Bouguer gravity anomaly (MBA) low and a peak in geochemical anomaly [e.g., *Verma and Schilling*, 1982; *Verma et al.*, 1983], suggesting anomalously thick crust and low density mantle related to the Galápagos plume (Figure 10). *Ito and Lin* [1995a, b] also found bathymetric and MBA anomalies along Cocos Plate isochrons, suggesting past plume influence on the paleo-Galápagos ridge axis. In the following section, we will first compare the along-isochron bathymetric plume widths with predictions of the above scaling laws to place theoretical constraints on the volume and buoyancy flux of the Galápagos plume. We will then examine observations and model predictions of along-isochron anomalies to investigate the possible temperatures and dimensions of the Galápagos plume source.

Along-Axis Plume Width

Ito and Lin [1995b] defined along-isochron widths of the Galápagos plume based on the lateral extent over which the observed bathymetry is shallower than depths predicted by the reference plate cooling model of *Carlson and Johnson* [1994], that is, depth = 2.6 km + 0.345 km m.y.$^{-1/2}$ $t^{1/2}$, where t is crustal age in million years. Along the present-day Galápagos ridge axis, the residual bathymetric width W is 970 km (Figures 10 and 11), which is similar to the geochemical anomaly width of 880 km [*Schilling*, 1991]. Along Cocos Plate isochrons of ages 2.6, 3.6, 6.0, 6.6, and 7.7 m.y., the residual bathymetric plume widths are 1250-1300 km (Figure 11). To associate a plume-ridge distance x_p to each isochron, we assumed the ridge axis was centered over the plume at ~10 Ma [*Hey*, 1977] and assumed a constant ridge migration rate from 10 Ma to present day. For example, the 3.6-Ma isochron was assumed to have formed when the plume was 36% closer to the ridge than it is today. We considered only Cocos Plate isochrons because they likely reflect crustal structure accreted only at the paleoridge axis, unlike the corresponding isochrons of the Nazca Plate which have been overprinted by off-axis hotspot volcanism.

Bathymetric anomaly widths are plotted versus paleoplume-ridge distance in Figure 11. We also show two curves derived from (14), which encompass the range of observed bathymetric widths. For the x_p values attributed to each isochron, (14) suggests the Galápagos plume has already attained its greatest possible width along the Galápagos ridge axis. Equation (14) also predicts that the Galápagos plume is capable of interacting with the ridge axis out to plume-ridge distances of 600-1000 km. Because (14) predicts W to increase with both γ (controlled by ΔT_p) and Q, a range of ΔT_p and plume flux values are investigated; ΔT_p of 50°C and Q of 1.6 x 10^7 km^3 m.y.$^{-1}$ yield the upper bound curve, while ΔT_p of 200°C and Q of 5.0 x 10^6 km^3 m.y.$^{-1}$ yield the lower bound curve. Although these two curves bracket a broad range of Q and ΔT_p values, they can be described by a relatively small range of buoyancy fluxes $B = Q\rho_0\alpha\Delta T$ of 2-2.5 x 10^3 kg s^{-1}. This result demonstrates the fact that while buoyancy flux is a useful measure of the strength of the Galápagos plume [e.g., *Sleep*, 1990; *Schilling*, 1991], it does not reveal plume volume flux or temperature anomaly independently. To further investigate Q and ΔT_p of the Galápagos plume, we next examine the possible processes leading to the amplitudes of the along-isochron bathymetric and gravity anomalies.

Calculations of Crustal Thickness, Topography, and Gravity

Here we examine a range of Galápagos models with plume source temperature anomalies of 50°-200°C. Because 70-75% of the along-isochron bathymetric and gravity variations may arise from plume-induced thickening of the igneous crust [*Ito and Lin*, 1995a], crustal thickness calculations are a crucial link between mantle fluid dynamic models and surface observations. To predict crustal thickness along a model ridge axis, we incorporated the solidus and liquidus functions of *McKenzie and Bickle* [1988], as well as their functional dependence of melt fraction M on homologous temperature for adiabatic batch melting. Similar to *Ito et al.* [1996], we assumed melt generated in the mantle accretes perpendicularly to the ridge axis to form crust. Our method generates a normal ridge crustal thickness of 6.5 km with an ambient potential temperature T_0 of 1300°C. However, because the Galápagos plume enhances

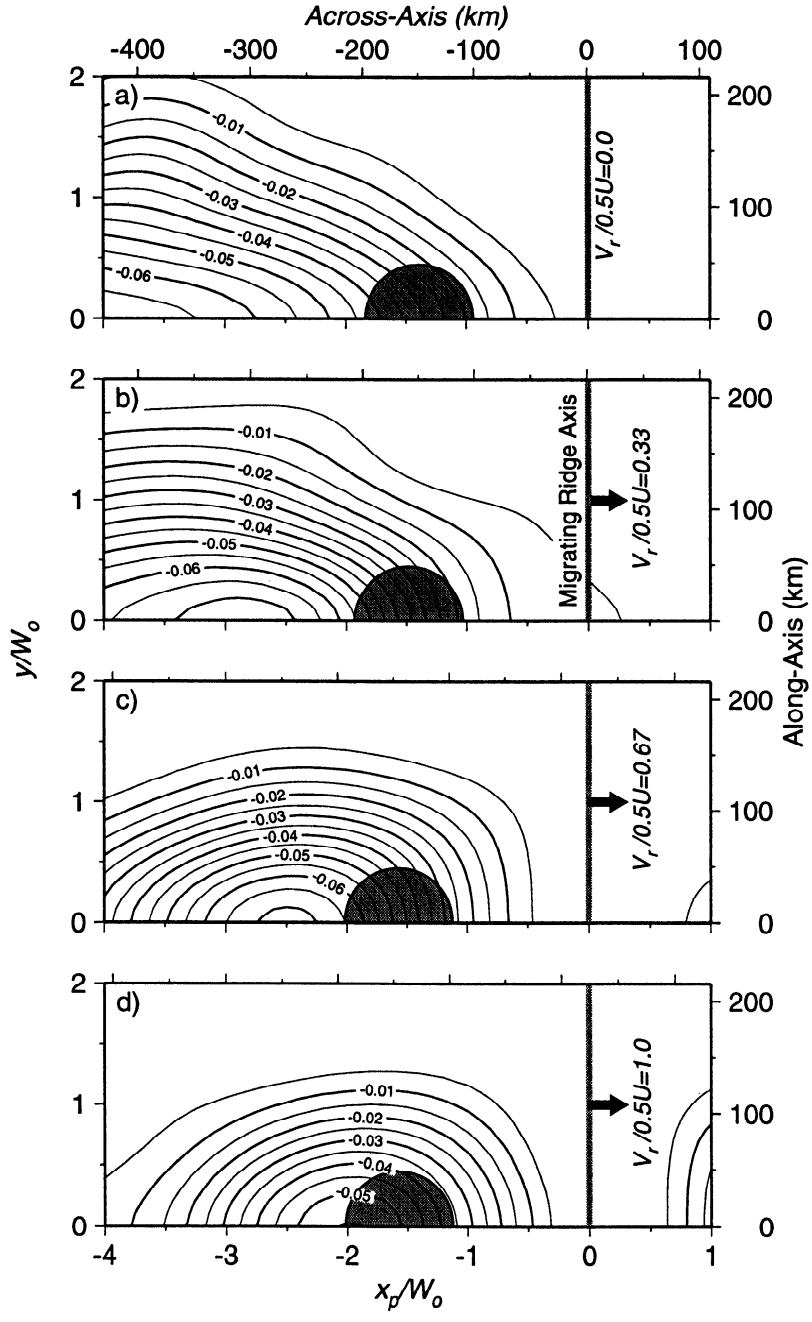

Figure 8. Contours of lithospheric erosional thickness, normalized by characteristic plume thickness S_0= 120 km, for experiment 8 with half spreading rate $0.5U$ = 30 km m.y.$^{-1}$ (Table 2). (a) $V_r/0.5U$ = 0.0 (steady state case), $x_p = x_{max}$ = -150 km, and x_p/W_0= -1.39. (b) $V_r/0.5U$ = 0.33, x_p = -160 km, and x_p/W_0 = -1.48; (c) $V_r/0.5U$ = 0.67, x_p = -170 km, and x_p/W_0= -1.57; and (d) $V_r/0.5U$ = 1.00, x_p = -170 km, and x_p/W_0= -1.57. Rheological boundary layer thickness is defined as the thickness over which $\eta/\eta_0 \geq 10$, and erosional thickness is the difference between plume-heated lithosphere and normal lithosphere. Ridge axis is marked by shaded vertical lines, and plume source is shown as shaded semicircles beneath plate 2.

crustal production at the ridge as well as generates the off-axis Galápagos Islands, an important source of uncertainty is how melt produced by the plume is partitioned between the ridge and off-axis islands. To date, there are no compelling models or constraints on the pattern of melt migration above plumes; therefore, we assumed that all melt generated closest to the ridge axis accretes at the Galápagos ridge axis, while melt generated closest to the plume source accretes at the Galápagos Islands.

When considering melting, it is important to account for its effects on the mantle [*Ito et al.* 1996]. Decompression melting reduces mantle potential temperature because of latent heat loss thereby increasing both mantle density and viscosity; while melt extraction reduces mantle density by depleting the residuum of iron with respect to magnesium [*Oxburgh and Parmentier*, 1977]. Similar to *Ito et al.* [1996], latent heat loss was incorporated by introducing a source term $-(T_R \Delta S/c_p)\dot{M}$ in the energy equation (equation (3)), where $\dot{M}$ is melting rate. The thermal and compositional effects on mantle density are described by

$$\Delta\rho = \rho_0(\alpha\Delta T + \beta X), \quad (16)$$

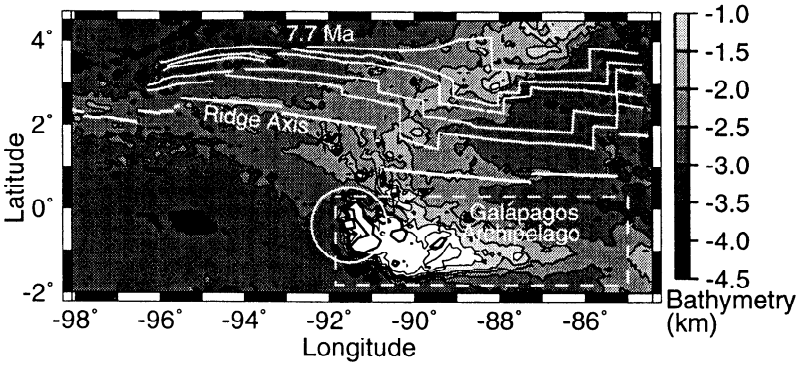

Figure 9. Bathymetry map of the Galápagos plume-ridge system based on shipboard and Etopo 5 bathymetry data of *Ito and Lin* [1995a]. White lines mark the present-day ridge axis and seafloor isochrons on the Cocos Plate with crustal ages of 2.6, 3.6, 6.0, 6.7, and 7.7 m.y. [*Wilson and Hey*, 1995]. The plume center is taken to be Fernandina Island as shown by the white circle with a radius of 100 km. The dashed box shows the region in which bathymetry was used to calculate the crustal volume flux of the Galápagos Archipelago.

where α is the coefficient of thermal expansion, X is the extent of melt depletion, and $\beta = 0.24$ is the coefficient of melt depletion-related density reduction [*Oxburgh and Parmentier*, 1977]. The equilibrium equation for the melt depletion field is

$$\frac{\partial X}{\partial t} = -\boldsymbol{u} \bullet \nabla X + \dot{M}, \tag{17}$$

in which the advection term was solved using the same tensor diffusion method as that used to solve for plume tracer field P.

To calculate isostatic topography, we considered contributions from both the crust and mantle. In calculating the crustal contribution to topography, we assumed Airy-type compensation of the crust with a normal density of 2800 kg m^{-3}. To account for the possible thickening of the higher density lower crust with increasing total crustal thickness [e.g., *Tolstoy et al.*, 1993; *White et al.*, 1992], we assumed that crustal density increases linearly from 2800 to 2900 kg m^{-3} within 500 km of the point closest to the hotspot (~91°W). In calculating the mantle contribution to topography, we assumed Pratt-type compensation with a compensation depth of 200 km and included both thermal and compositional density effects as defined in (16).

The mantle-Bouguer gravity anomaly (MBA) is the free-air gravity minus the attraction due to seafloor topography and crust-mantle interface, assuming a crust of uniform density and thickness [e.g., *Kuo and Forsyth*, 1988; *Lin et al.*, 1990]. The

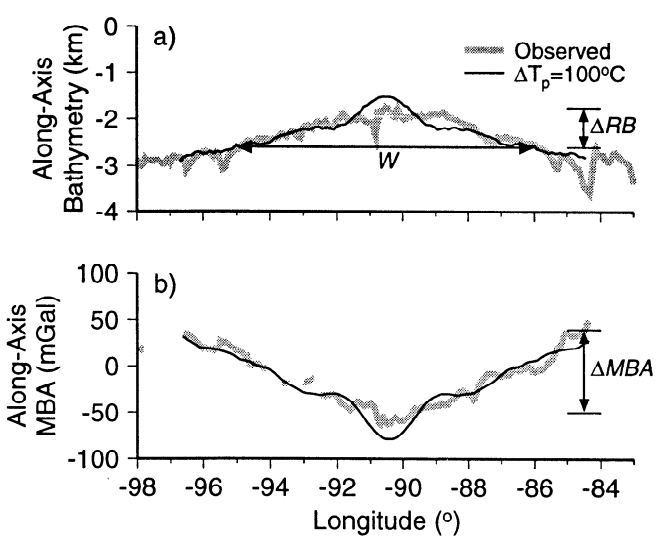

Figure 10. The observed profiles (shaded lines) of (a) bathymetry and (b) mantle-Bouguer gravity anomaly (MBA) along the present-day ridge axis [*Ito and Lin*, 1995a] are compared with the predicted profiles (solid lines) based on model 2 with ΔT_p = 100°C (Table 3). The amplitude of residual bathymetric anomaly ΔRB is the total along-axis bathymetric variation in excess of the seafloor depth predicted by a reference cooling plate model. This reference depth also defines along-axis anomaly width W. The amplitude of mantle-Bouguer gravity anomaly ΔMBA denotes its total along-axis variation. The bulge in the predicted anomaly at ~91°W reflects enhanced crustal thickness caused by rapid upwelling and thus melting rates over the plume source. The more gradual slopes at distances >~100 km away from 91°W reflects along-axis mantle temperature gradients and small differences in upwelling rate. Note that our models do not include the 91°W transform fault. We anticipate its largest effect is to reduce melting near the cool ends of the adjoining segments and to cause asymmetry in crustal thickness because of the ~100 km offset of the two adjacent segments. However, neither of these two effects is evident in the along-axis bathymetric, gravity, or geochemical anomalies [e.g., Verma *and Schilling*, 1982; *Verma et al.*, 1983] .

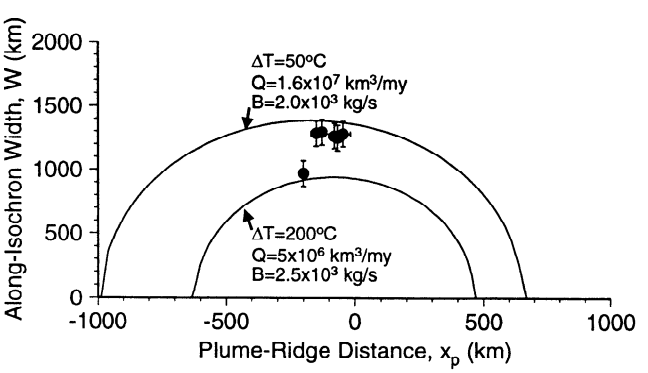

Figure 11. The observed along-isochron bathymetric anomaly width W versus the estimated paleoplume-ridge distance for the Galápagos system for various crustal ages over the past 7.7 m.y. Also shown are two example predictions based on equation (14) (solid curves).

Table 3. Galápagos Plume Models

Model	ΔT_p, °C	Source Radius, km	Q, 10^6 km^3 m.y.$^{-1}$	B, 10^3 kg s^{-1}	Crustal Thickness Anomaly, km	Contribution to Anomalies by Crust, %	Maximum Melt Fraction
1	50	200	9.1	1.2	3.2- 5.3	60-80	0.21
2	100	100	6.0	1.5	4.8-12.4	60-80	0.25
3	150	80	6.0	2.3	4.8-21.0	50-85	0.29
4	200	60	4.7	2.4	2.7-27.0	30-85	0.31

Numerical box dimensions are 1280 x 800 x 400 km with 128 x 64 x 50 grids in x, y, and z, respectively. Assumed values for T_0 of 1300°C and η_0 of 3 x 10^{19} Pa s yield a Rayleigh number of 3.05 x 10^6. Model inputs are ΔT_p and source radius; model outputs are the remaining quantities. Listed crustal thickness anomalies are the axial crustal thickness in excess of 6.5 km along the present-day ridge and along the 7.7-m.y. isochron, respectively. Listed percents of anomalies due to the crust are values along the present-day ridge and the 7.7-m.y. isochron, respectively. Maximum melt fraction is the predicted maximum extent of melting of ridge axis melts. Melting directly over the plume source (i.e. melts partitioned to the off-axis islands) acheived approximately half of the above listed degrees of melting.

MBA thus reflects lateral variations in crustal thickness and/or mantle and crustal density structure. To predict MBA from our models, we again included the contributions of the predicted along-isochron crustal thickness variations and thermal and compositional mantle density variations from (16).

We examined four Galápagos plume source temperature anomalies of 50°, 100°, 150°, and 200°C (Table 3). Plume source radii were set independently such that plume volume fluxes were sufficiently high (5-9 x10^6 km^3 m.y.$^{-1}$) to generate plume widths consistent with the residual bathymetric width along the present-day ridge axis. Consequently, the cooler, less buoyant plumes required broader sources to obtain the same volume fluxes as the hotter, more buoyant, and narrower plume sources. Plume source radii were <15% of the along-axis widths and therefore imposed minimal effect on the dynamics of the system. We began model calculations with a steady state condition of the plume beneath plate 1 (Cocos Plate); we then activated ridge migration and tracked crustal production as the ridge migrated over the plume source. Calculations finished with plate 2 (the Nazca Plate) over the plume source and when the ridge was 200 km from the plume source.

Along-Isochron Bathymetric and Gravity Anomalies

The observed bathymetric and MBA profiles along the ridge axis are shown in Figure 10 with an example set of the predicted profiles from model 2 (ΔT_p = 100°C). The amplitudes and widths of the predicted anomalies are consistent with the observed along-axis anomalies. Models 1, 3, and 4 also yield predictions consistent with the present-day ridge axis anomalies. In Figure 12, we show the amplitudes of the predicted and observed residual bathymetry (ΔRB) and mantle-Bouguer anomalies (ΔMBA) plotted versus isochron age and x_p. The predicted bathymetric anomalies and MBA along the Cocos Plate isochrons are the combined contributions from the along-axis crustal thickness variations generated at corresponding values of x_p and mantle density variations at the associated x positions on plate 1. Along the three youngest isochrons associated with the greatest values of x_p, all four model profiles show reasonable agreement with the observed amplitudes. Along the three oldest isochrons associated with the smallest values of x_p, however, models 3 and 4 (ΔT_p = 150° and 200°C, respectively) predict amplitudes significantly greater than the observations, whereas models 1 and 2 (ΔT_p = 50° and 100°C, respectively) yield predictions more consistent with the observations.

The differences in shapes of the curves in Figure 12 illustrate the sensitivity of ΔRB and ΔMBA to plume source radius and temperature. The dependence of ΔRB and ΔMBA on x_p reflect variations in axial melting rate (i.e., crustal thickness) which depends primarily on upwelling rate beneath the ridge axis. Upwelling rate is predicted to be most rapid when the ridge is over the plumes source center and predicted to decrease with increasing x_p (Figure 12c). This decrease in upwelling rate with increasing x_p is most dramatic for the hottest sources with the narrowest radii. For example, in model 4 with ΔT_p = 200°C, upwelling rate is predicted to decrease by an order of magnitude from the source center to a radial distance of ~100 km (Figure 12c). This large change in upwelling rate causes a marked decrease in predicted crustal thickness anomaly from 27 km along the 7.7.-m.y. isochron to 2.7 km along the present-day ridge axis (Table 3), resulting in a large decrease in predicted anomaly amplitudes. In contrast, in the coolest and broadest source of model 1, upwelling rate is predicted to decrease by only 20% within 100 km of the source center. The corresponding reduction in crustal thickness is < 2 km from 7.7 Ma to the present-day ridge axis, resulting in only a small decrease in anomaly amplitudes with increasing x_p. The relatively moderate variation in the observed ΔRB and ΔMBA with x_p is consistent with a Galápagos plume of mild temperature anomaly (ΔT_p = 50°-100°C) and moderate radius (100-200 km). Models 1 and 2 predict crustal thickness anomalies of 3.2-4.8 km at the present-day ridge axis, a result that is consistent with previous predictions of *Ito and Lin* [1995a, b].

Galápagos Archipelago Crustal Volume Flux

Because of the uncertainty in how melt is partitioned between the ridge axis crust and hotspot islands, we also estimated the rate of crustal production at the Galápagos Archipelago. The bathymetry in the white box in Figure 9 was considered, the longitudinal extent of which corresponds to ~10 m.y. of island accretion [*Sinton et al.*, 1996]. After subtracting the long wavelength swell topography, we calculated the isostatic crustal thickness of the Galápagos Archipelago by assuming Airy isostasy and crustal densities of 2800-3000 kg m^{-3}. Excess crustal volume was then derived (the thickness of a normal oceanic crust of 6.5 km excluded) as a function of longitude across the white box of Figure 9 and each longitudi-

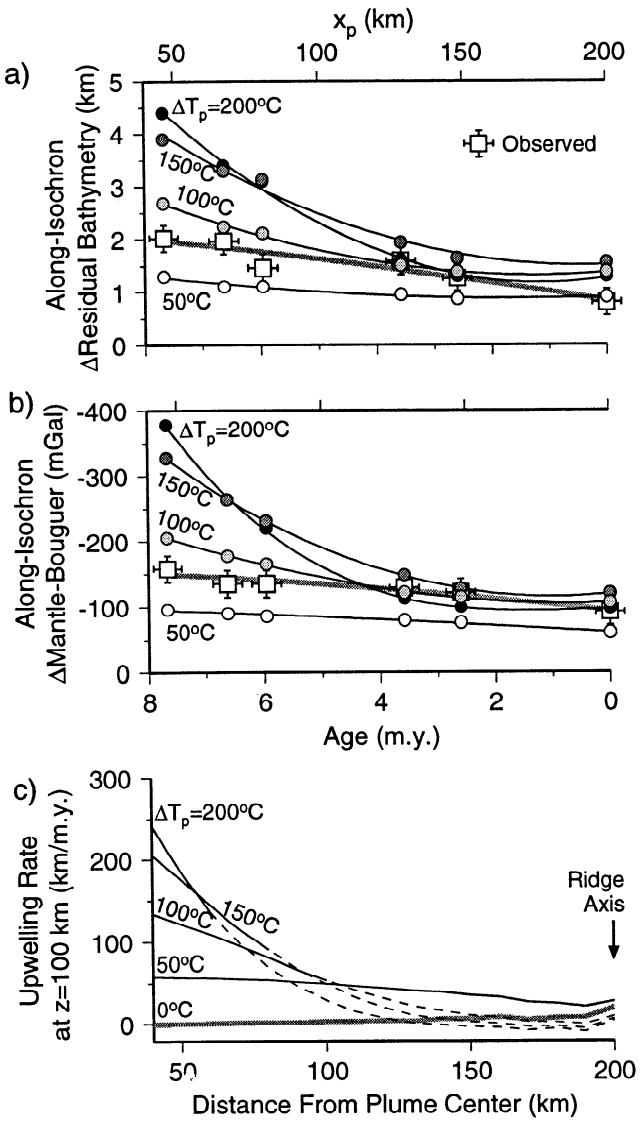

Figure 12. The observed amplitudes of along-isochron variations (squares) in (a) residual bathymetry and (b) MBA are plotted versus isochron age and paleoplume-ridge distance. Thick shaded curves are best fitting polynomial functions of the data. Also shown are predicted anomaly amplitudes of the four plume source models of Table 3 (shaded circles) and their best fitting curves (solid lines). (c) The predicted mantle upwelling rate at z = 100 km of the four plume source models for x_p = 200 km (Table 3). These profiles were taken along ridge-perpendicular transects from the plume center northward to the ridge axis. The solid portions of the curves show the extents of the plume source radii, while the dashed portions are outside of the source radii. The curve of ΔT_p = 0°C (shaded) shows normal ridge upwelling rate without a plume.

nal value was assigned an age assuming a constant migration rate of the Nazca Plate relative to the plume. Finally, we estimated crustal volume flux through time by dividing the estimated volumes by the time spans represented by their spacing in longitude.

The above calculations yield island crustal fluxes of 0.3-3 x 10^5 km^3 m.y.$^{-1}$ with an average of 1.3 x 10^5 km^3 m.y.$^{-1}$ over the past 8 m.y. These flux estimates are compared with those predicted from the numerical models in Figure 13. The two hotter plume source models over predict the island crustal fluxes, while the two cooler models are more consistent with the estimated island fluxes. Consistent with the results of along-isochron anomalies, these island crustal flux comparisons also suggest a mild temperature anomaly (~50°-100°C) for the Galápagos plume. We note, however, that our models assume a steady state plume source, whereas some of the variations in the along-axis anomalies and island crustal fluxes may have resulted from a time-dependent Galápagos plume source. For example, the low values of observed along-axis anomalies and island crustal volume fluxes relative to the predictions of model 2 for times >4 Ma are consistent with a cooler Galápagos source temperature in the past.

Geochemical Implications

Many of the original observations that led to the concept of ridge-feeding plumes were derived from systematic variations in basalt chemistry. Galápagos ridge axis basalts erupted near the Galápagos hotspot have compositional affinities to ocean island basalts (OIB), being enriched relative to mid-ocean ridge basalts (MORB) in radiogenic isotopes [*Verma and Schilling*, 1982; *Verma et al.*, 1983] and incompatible rare earth and major elements [*Schilling et al.*, 1976; *Schilling et al.*, 1982]. *Verma and Schilling* [1982] and *Verma et al.* [1983] showed that the OIB signatures decrease along the ridge axis with increasing distance from the hotspot as reflected in La/Sm variations in Figure 14. Such a systematic decrease in the OIB signature is interpreted to reflect mixing between the OIB plume source with the MORB upper mantle source material.

To investigate the mixing process between plume and ambient mantle, we calculated the amount of plume tracer P in melts accreted along the ridge axis. After *Ito et al.* [1996], the average plume tracer concentration in accumulated melts as a function of along-axis coordinate is

$$\overline{P}(y) = \frac{\int P(x,y,z)\dot{M}(x,y,z)\mathrm{d}x\mathrm{d}z}{\int \dot{M}(x,y,z)\mathrm{d}x\mathrm{d}z}. \qquad (18)$$

$\overline{P}$ = 1.0 indicates that all melts generated in a plane perpen-

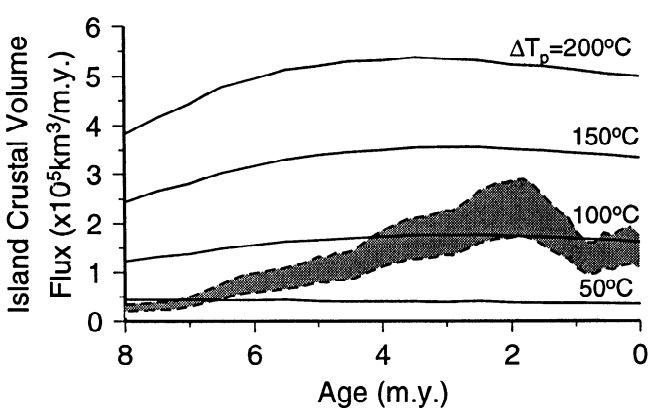

Figure 13. Estimates of crustal volume flux of the Galápagos Archipelago assuming isostatic compensation of island topography are plotted versus crustal age. Upper dashed curve is calculated assuming a crustal density of 3000 kg m^{-3}, and lower dashed curve is calculated assuming a crustal density of 2800 kg m^{-3}. Also shown are predictions (solid lines) based on the four plume source models of Table 3 labeled with their source temperature anomalies.

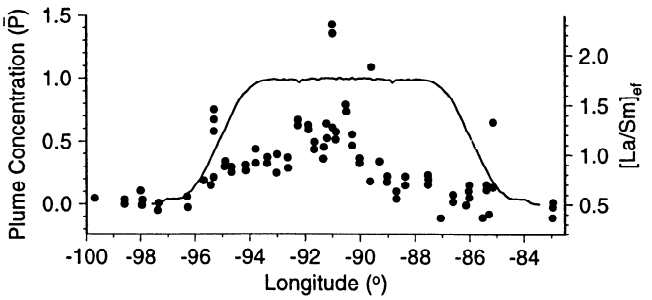

Figure 14. The observed along-axis variations in $[La/Sm]_{ef}$ (circles) from *Schilling et al.* [1982] are compared with the predicted along-axis profile of plume tracer concentration $\bar{P}$ (solid line) for model 2 with ΔT_p = 100°C and plume source radius = 100 km (Table 3). The absolute values of $\bar{P}$ relative to the absolute values of $[La/Sm]_{ef}$ are arbitrary.

dicular to that point of the ridge are entirely plume-source derived. Likewise, $\bar{P}$ = 0.0 indicates that none of the melts are plume-derived, and 0.0 < $\bar{P}$ < 1.0 indicates some of the melts are plume-derived and the rest are ambient mantle-derived.

Results from example calculations of model 2 (Figure 14) show that the predicted geochemical plume width is consistent with the ~1000 km width of the observed La/Sm anomaly. The largest discrepancy predicted by the model profile is that it indicates very little mixing between the plume-derived and ambient mantle-derived melts over most of the plume-affected portions of the ridge axis. Only at the outermost ~200 km within the edges of the plume does the model suggest plume-ambient source mixing. An explanation for such a discrepancy, which we also noted for Iceland [*Ito et al.*, 1996], is that mixing may not occur in the shallow mantle or in the crust but, instead, occurs deeper in the mantle than we have considered in our models. Such a deep mixing process may be entrainment of the ambient mantle material by the plume as it ascends through the isotopically depleted region of the mantle [e.g., *Geist et al.*, 1988; *Graham et al.*, 1993].

Discussion

The above plume-migrating ridge models can explain the first-order along-isochron anomalies of the Cocos Plate over the past ~8 m.y. as well as Galápagos island volume fluxes. Our predicted plume source temperature anomalies (50°-100°C) are significantly less than previous estimates of the Galápagos plume (~200°C) [e.g., *Sleep*, 1990; *Schilling*, 1991]. The most important difference between our model predictions and the previous estimates is that our models consider both crustal and mantle effects, whereas the previous estimates focused primarily on mantle density variations. An important assumption in our models, however, is that melt migration along the ridge axis is small or nonexistent. If, instead, along-axis melt migration is significant, the Galápagos plume source may be hotter and narrower than our models suggest [*Ito et al.*, 1996].

As noted earlier, mild plume temperature anomalies also imply low "upslope numbers" $\Pi_u = Q^{1/8}\sigma^{3/8}\kappa^{1/2}/0.5U$, suggesting that variations in lithospheric thickness are insignificant to the dynamic behavior of the Galápagos mantle plume. As demonstrated in the high-Π_u theoretical experiments of *Sleep* [1996] (Π_u = 5-13), systems in which the lithosphere effectively channels plume material to and along the ridge require more buoyant and/or less viscous plumes than those we have modeled. If this is the case for the Galápagos, then our models would predict substantially higher melting rates than even our high-ΔT_p models and thus yield large overpredictions to the along-isochron anomalies as well as the island crustal volume fluxes. Thus, if in fact the Galápagos plume is sufficiently hot and low in viscosity to be channeled by overlying lithosphere, then we would be left to reconcile predicted crustal production rates significantly greater than those inferred from the observed geophysical anomalies of the Cocos Plate and the Galápagos Archipelago.

A potentially effective test of the mild-versus-hotter plume source models is a mantle seismic tomographic study of the Galápagos plume-ridge system, which would provide constraints on plume source dimension and temperature anomaly. Beneath the Galápagos Archipelago, our models predict *P* wave velocity reduction of 0.5-0.7% due to the excess temperature of the plume and up to 2% in the melting region if there is up to 3% of melts retained in the mantle (based on 6.25 x 10^{-3}% reduction of *P* wave velocity for each 1°C temperature anomaly and 1.25% decrease in velocity for each 1% porosity of melts in the mantle [*Humphreys and Dueker*, 1994]). Such velocity anomalies are predicted to result in a 0.3-0.4 s delay over the center of the hotspot for *P* waves passing vertically through the upper 400 km of mantle. Beneath the Galápagos ridge axis, however, our models predict mantle *P* wave velocities in the melting zone to actually increase near the plume by up to 0.5% relative to normal subaxial velocities. This is because the plume material feeding the ridge has already experienced melting at the hotspot; consequently, the velocity-enhancing effect of melt depletion (0.1% velocity increase for each 1% degree of depletion [*Humphreys and Dueker*, 1994]) is predicted to dominate over the velocity-reducing effects of temperature and melt retention directly beneath the ridge. Another valuable study would be to obtain direct seismic constraints on crustal structure along the ridge axis and along seafloor isochrons.

Additional complexities that may affect along-axis plume width *W* and maximum plume-ridge interaction distance x_{max} include ridge jumps and asymmetric plate spreading. Episodes in which the ridge jumps toward the neighboring plume have been documented for the Galápagos system [*Wilson and Hey*, 1995] as well as other systems in the southern oceans [*Small*, 1995]. Such episodes may result directly from plume-ridge interaction as the plume weakens the overlying plate near the ridge [*Small*, 1995]. Asymmetrically spreading ridges, which may also result directly from plume weakening of the lithosphere, have been suggested to be common to plume-ridge systems [*Small*, 1995]. These two factors, however, are predicted to have little affect on x_{max} when a ridge migrates toward a plume source because x_{max} in this case is controlled by the stagnation point of the plume rather than motion of the ridge. On the other hand, ridge jumps and asymmetric spreading may increase x_{max} significantly when a ridge migrates away from a plume source because x_{max}, in this second case, is determined by the point at which the migrating ridge outruns the ridgeward spreading plume.

The above scaling laws of along-axis plume width *W* suggest that plumes affect broad regions of oceanic plates, especially at slow spreading plates. Equations (14) and (15) predict that the maximum along-axis width of a plume is 125-200% as broad as the maximum plume-ridge interaction distance. In the Atlantic and southern oceans, where plume sig-

natures are identified at ridges as far as 1400 km away from plume sources, the scaling laws imply that individual plumes may spread over distances of up to 2500 km along seafloor isochrons. The resulting large regions of plume-affected lithosphere may contribute to the formation of "tectonic corridors" as identified by *Kane and Hayes* [1992] and *Hayes and Kane* [1994]. Among the most prominent examples of plume-affected lithosphere are the broad regions of anomalously shallow seafloor associated with the Galápagos plume as discussed in this study, the Iceland and Azores plumes in the North Atlantic, the Tristan plume in the South Atlantic, and the Kerguelen and Marion plumes in the Indian Ocean. Such a scenario suggests that plumes may be a major source of lithospheric accretion as proposed by *Phipps Morgan and Smith* [1992] and *Phipps Morgan et al.* [1995].

Conclusions

Our numerical results predict that along-axis plume width W and maximum distance of plume-ridge interaction x_{max} scale with $(Q/U)^{1/2}$, where Q is plume source volume flux and U is ridge full spreading rate. Both W and x_{max} increase with buoyancy number Π_b, which reflects the strength of gravitational- versus plate-driven spreading. These scaling laws derived for steady state stationary ridges are consistent with those obtained from independent studies of *Ribe* [1996]. In the case of a migrating ridge, the distance of plume-ridge interaction is reduced when the ridge migrates toward the plume because of the excess drag of the leading plate and is enhanced when the ridge migrates away from the plume because of the reduced drag of the slower moving trailing plate. The slope of the lithospheric boundary layer and thermal erosion of the lithosphere have little effect on plume flow for the mildly buoyant and relatively viscous plumes here investigated. Our models suggest that mantle plumes may spread along crustal isochrons over distances 125-200% broader than the maximum distance to which they interact with ridges. Plumes may therefore compose a significant percentage of the oceanic lithosphere.

On the basis of scaling laws for W, the observed along-isochron plume widths of the Galápagos system suggest mantle plume volume fluxes of 5-16 x 10^6 km^3 $m.y.^{-1}$ and a buoyancy flux of ~2 x 10^3 kg s^{-1}. The observed increases in along-isochron residual bathymetric and mantle-Bouguer gravity anomalies with increasing isochron age can be explained by increased crustal thickness generated at the paleoridge axis. The primary factor controlling melt production rate is the rate of upwelling in the axial melting zone, which is predicted to be greater in the past when the ridge was closer to the Galápagos plume source. The amplitudes of the along-isochron bathymetric and mantle-Bouguer gravity anomalies are best explained by a plume source with a relatively mild temperature anomaly (50°-100°C) and moderate radius (100-200 km). Furthermore, the same plume source models predict crustal production rates at the Galápagos Archipelago that are consistent with estimations of off-axis island crustal fluxes. Predictions of the along-axis geochemical signature of the Galápagos plume suggest that mixing between the plume OIB and ambient MORB sources may not occur in the asthenosphere but, instead, may occur deeper in the mantle possibly by entrainment of depleted mantle as the plume ascends from its source.

Acknowledgments. This study was funded by NSF grant OCE-9302915 and the SOEST Young Investigator Program. We thank R. Detrick, M. McNutt, J.-G. Schilling, and J. Whitehead for their constructive comments and D. Geist, S. King, and C. Small for their thorough reviews of this manuscript. The GMT software [*Wessel and Smith*, 1995] was used extensively. Woods Hole Oceanographic Institution contribution 9383.

References

Carlson, R. L., and H. P. Johnson, On modeling the thermal evolution of the oceanic upper mantle: An assessment of the cooling plate model, *J. Geophys. Res.*, *99*, 3201-3214, 1994.

Christensen, U., Convection with pressure- and temperature-dependent non-Newtonian rheology, *Geophys. J. R. Astron. Soc*, *77*, 343-384, 1984.

DeMets, C., R. G. Gordon, D. F. Argus, and S. Stein, Effect of recent revisions to the geomagnetic reversal time scale on estimates of current plate motions, *Geophys. Res. Lett.*, *21*, 2191-2194, 1994.

Feighner, M. A., and M. A. Richards, The fluid dynamics of plume-ridge and plume-plate interactions: An experimental investigation, *Earth Planet. Sci. Lett.*, *129*, 171-182, 1995.

Feighner, M. A., L. H. Kellogg, and B. J. Travis, Numerical modeling of chemically buoyant mantle plumes at spreading ridges, *Geophys. Res. Lett.*, *22*, 715-718, 1995.

Gable, C. W., Numerical models of plate tectonics and mantle convection in three dimensions, Ph.D. thesis, Harvard Univ., Cambridge Mass., 1989.

Gable, C. W., R. J. O'Connel, and B. J. Travis, Convection in three dimensions with surface plates: Generation of toroidal flow, *J. Geophys. Res.*, *96*, 8391-8405, 1991.

Geist, D. J., W. M. White, and A. R. McBirney, Plume-asthenosphere mixing beneath the Galapagos archipelago, *Nature*, *333*, 657-660, 1988.

Graham, D. W., D. M. Christie, K. S. Harpp, and J. E. Lupton, Mantle plume Helium in submarine basalts from the Galápagos platform, *Science*, *262*, 2023-2026, 1993.

Gripp, A. E., and R. G. Gordon, Current plate velocities relative to the hotspots incorporating the NUVEL-1 global plate motion model, *Geophys. Res. Lett.*, *17*, 1109-1112, 1990.

Hayes, D. E., and K. A. Kane, Long-lived mid-ocean ridge segmentation of the Pacific-Antarctic ridge and the Southeast Indian ridge, *J. Geophys. Res.*, *99*, 19,679-19,692, 1994.

Hey, R., Tectonic evolution of the Cocos-Nazca spreading center, *Geol. Soc. Am. Bull.*, *88*, 1404-1420, 1977.

Humphreys, E. D., and K. G. Dueker, Physical state of the western U.S. upper mantle, *J. Geophys. Res.*, *99*, 9635-9650, 1994.

Ito, G., and J. Lin, Mantle temperature anomalies along the present and paleoaxes of the Galápagos Spreading Center as inferred from gravity analyses, *J. Geophys. Res.*, *100*, 3733-3745, 1995a.

Ito, G., and J. Lin, Oceanic spreading center-hotspot interactions: Constraints from along-isochron bathymetric and gravity anomalies, *Geology*, *23*, 657-660, 1995b.

Ito, G., J. Lin, and C. W. Gable, Dynamics of mantle flow and melting at a ridge-centered hotspot: Iceland and the Mid-Atlantic Ridge, *Earth Planet. Sci. Lett.*, *144*, 53-74, 1996.

Kane, K. A., and D. E. Hayes, Tectonic corridors in the South Atlantic: Evidence for long-lived mid-ocean ridge segmentation, *J. Geophys. Res.*, *97*, 17,317-17,330, 1992.

Kincaid, C., G. Ito, and C. Gable, Laboratory investigation of the interaction of off-axis mantle plumes and spreading centres, *Nature*, *376*, 758-761, 1995a.

Kincaid, C., J.-G. Schilling, and C. Gable, The dynamics of off-axis plume-ridge interaction in the uppermost mantle, *Earth Planet. Sci. Lett.*, *137*, 29-43, 1995b.

Kuo, B.-Y., and D. W. Forsyth, Gravity anomalies of the ridge-transform system in the South Atlantic between 31° and 34.5°S: Upwelling centers and variations in crustal thickness, *Mar. Geophys. Res.*, *10*, 205-232, 1988.

Lin, J., G. M. Purdy, H. Schouten, J.-C. Sempéré, and C. Zervas, Evidence from gravity data for focused magmatic accretion along the Mid-Atlantic Ridge, *Nature*, *344*, 627-632, 1990.

McKenzie, D., and M. J. Bickle, The volume and composition of melt generated by extension of the lithosphere, *J. Petrol.*, *29*, 625-679, 1988.

Morgan, W. J., Rodriguez, Darwin, Amsterdam,..., A second type of hotspot island, *J. Geophys. Res.*, *83*, 5355-5360, 1978.

Oxburgh, E. R., and E. M. Parmentier, Compositional and density stratification in oceanic lithosphere—Causes and consequences, *J. Geol. Soc. London*, *133*, 343-355, 1977.

Phipps Morgan, J., and W. H. F. Smith, Flattening of the sea-floor depth-age curve as a response to asthenospheric flow, *Nature*, *359*, 524-527, 1992.

Phipps Morgan, J., W. J. Morgan, Y.-S. Zhang, and W. H. F. Smith, Observational hints for a plume-fed, suboceanic asthenosphere and its role in mantle convection, *J. Geophys. Res.*, *100*, 12,753-12,767, 1995.

Ribe, N., The dynamics of plume-ridge interaction, 2, Off-ridge plumes, *J. Geophys. Res.*, *101*, 16,195-16,204, 1996.

Ribe, N., and W. L. Delattre, The effect of ridge migration on plume-ridge interaction (abstract), *Eos Trans. AGU*, *77* (46), Fall Meet. Suppl., F730-F731, 1996.

Ribe, N., U. R. Christensen, and J. Theissing, The dynamics of plume-ridge interaction, 1: Ridge-centered plumes, *Earth Planet. Sci. Lett.*, *134*, 155-168, 1995.

Schilling, J.-G., Iceland mantle plume: Geochemical study of Reykjanes Ridge, *Nature*, *242*, 565-571, 1973.

Schilling, J.-G., Upper mantle heterogeneities and dynamics, *Nature*, *314*, 62-67, 1985.

Schilling, J.-G., Fluxes and excess temperatures of mantle plumes inferred from their interaction with migrating mid-ocean ridges, *Nature*, *352*, 397-403, 1991.

Schilling, J.-G., R. N. Anderson, and P. Vogt, Rare earth, Fe and Ti variations along the Galapagos spreading centre, and their relationship to the Galapagos mantle plume, *Nature*, *261*, 108-113, 1976.

Schilling, J.-G., R. H. Kingsley, and J. D. Devine, Galapagos hot spot-spreading center system, 1, Spatial petrological and geochemical variations (83°W-101°W), *J. Geophys. Res.*, *87*, 5593-5610, 1982.

Schilling, J.-G., G. Thompson, R. Kingsley, and S. Humphris, Hotspot-migrating ridge interaction in the South Atlantic, *Nature*, *313*, 187-191, 1985.

Sinton, C. W., D. M. Christie, and R. A. Duncan, Geochronology of the Galápagos seamounts, *J. Geophys. Res.*, *101*, 13,689-13,700, 1996.

Sleep, N. H., Hot spots and mantle plumes: Some phenomenology, *J. Geophys. Res.*, *95*, 6715-6736, 1990.

Sleep, N., Lateral flow of hot plume material ponded at sublithospheric depths, *J. Geophys. Res.*, 101, 28,065-28,083, 1996.

Small, C., Observations of ridge-hotspot interactions in the Southern Ocean, *J. Geophys. Res.*, *100*, 17,931-17,946, 1995.

Tolstoy, M., A. J. Harding, and J. A. Orcutt, Crustal thickness on the Mid-Atlantic ridge: bull's eye gravity anomalies and focused accretion, *Science*, 262, 726-729, 1993.

Travis, B., P. Olson, and G. Schubert, The transition from two-dimensional to three-dimensional planforms in infinite-Prandtl-number thermal convection, *J. Fluid Mech.*, *216*, 71-91, 1990.

Verma, S. P., and J.-G. Schilling, Galapagos hot spot-spreading center system, 2, $^{87}Sr/^{86}Sr$ and large ion lithophile element variations (85°W-101°W), *J. Geophys. Res.*, *87*, 10,838-10,856, 1982.

Verma, S. P., J.-G. Schilling, and D. G. Waggoner, Neodymium isotopic evidence for Galapagos hotspot-spreading centre system evolution, *Nature*, *306*, 654-657, 1983.

Vogt, P. R., Asthenosphere motion recorded by the by the ocean floor south of Iceland, *Earth Planet. Sci. Lett.*, *13*, 153-160, 1971.

Wessel, P., and W. H. F Smith, New version of the Generic Mapping Tools released, *Eos Trans. AGU*, *76*, 329, 1995.

White, R. S., D. McKenzie, and R. K. O'Nions, Oceanic crustal thickness from seismic measurements and rare earth element inversions, *J. Geophys. Res.*, 97, 19,683-19,715, 1992.

Wilson, D. S., and R. N. Hey, History of rift propagation and magnetization intensity for the Cocos-Nazca spreading center, *J. Geophys. Res.*, *100*, 10,041-10,056, 1995.

C. W. Gable, Earth and Environmental Sciences, Los Alamos National Laboratories, Los Alamos, NM 87545. (email: gable@lanl.gov)

G. Ito, Department of Geology and Geophysics, 2525 Correa Road, University of Hawaii, Honolulu, HI, 96822. (email: gito@soest.hawaii.edu)

J. Lin, Department of Geology and Geophysics, Woods Hole Oceanographic Institution, Woods Hole, MA 02543. (email: jlin@whoi.edu)

(Received November 14, 1996; revised March 15, 1997;
accepted April 8, 1997.)